Research in Zoology 2020, 10(1): 18-30
DOI: 10.5923/j.zoology.20201001.03

Hydrodynamic Impacts of Prominent Longitudinal Ridges on the 'Whale Shark' Swimming

Arash Taheri

Ph.D., Division of Applied Computational Fluid Dynamics, Biomimetic and Bionic Design Group, Tehran, Iran

Abstract Interaction between an animal and its habitat is one of the crucial factors in the evolution process. In aquatic environments, marine species have developed some unique morphological features with hydrodynamic consequences to overcome necessity of life over the course of million years. In this paper, hydrodynamic effects of the longitudinal-dorsal ridges covering the upper-lateral sides of whale shark's body as a prominent eidonomic characteristic of these species are studied with the aid of computational fluid dynamics (CFD). In this regard, flow physics of the problem is numerically simulated at high Reynolds number, i.e. 1.4×10^7 corresponding to the swimming of a 10 meter-whale shark at its average speed, i.e. $5 km/h$, using Lam-Bremhorst turbulence model. The results indicate that presence of the longitudinal ridges leads to formation of streamwise vortices which delays flow separation on the body and modifies hydrodynamic characteristics of the whale shark swimming. At sideslip angles, flow simulation results show that the ridges noticeably contribute to the 'sinking feeling' of the animal. Furthermore, spectral analysis of the unsteady simulation results in start-up phase of the whale shark's tail beating in a quiescent flow environment depict that these morphological features uniformize energy content of the vortical structures originating from the tail/caudal peduncle (not caudal fin) via suppressing of its energy peaks.

Keywords Whale sharks, Ridges, Functional morphology, Locomotion, Hydrodynamics, CFD, Ichthyology, Bionics

1. Introduction

Whale sharks (*Rhincodon typus*) are the largest fish in the world that slowly swim in tropical open waters including oceans, seas and gulfs (Fig. 1). Mexico [1], Australia [2] and Philippines [3] possess largest known populations of these highly migratory marine species, although they can be widely found in all regions with tropical waters with relatively high temperature like Taiwan [4] and Indonesia [5]. Persian Gulf (*Khalij-e Fars*) at the south of Iran with its warmest ocean water on the planet hosts numerous species of this amazing animal during summer and winter seasons in zones with depths greater than 40 m [6].

Whale sharks have evolved a perfect streamlined body possessing pairs of pectoral, pelvic and dorsal fins, as well as one anal and one vertical caudal fin (Fig. 2). As one can see in the eidonomy of the animal, undoubtedly the most pronounced feature of its morphology for any viewer could be presence of the prominent ridges on the upper part, i.e. lateral and dorsal sections, of the marine animal (Fig. 1, 2). Whale sharks are born with a total length of 55-64 cm; mature ones have a total length of greater than 6 and 8 meters for male and female species, respectively [7]. Maximum total length of these giant filter-feeding sharks can reach to 17-21.4 meters [7,8].

Figure 1. Whale shark swimming in Indian Ocean [21]; red dashed line window: a zone typically adopted for identification of species [9]

In contrast to whales that are breath-holding animals and do not have a gill, sharks including whale sharks have a gill and take oxygen from water for metabolism. It is also interesting to mention that white spot and stripe checkerboard patterns on the skin of whale sharks (Fig. 1) is a unique sign of any individual whale shark specie, similar to fingerprints for human being. This characteristic can be adopted along with artificial intelligence techniques, e.g. pattern recognition methods, to identify whale shark

* Corresponding author:
taha.bionics@gmail.com (Arash Taheri)
Received: July 5, 2020; Accepted: August 7, 2020; Published: August 15, 2020
Published online at http://journal.sapub.org/zoology

individuals [2,9]. In this regard, photo of spot patterns in a window behind the whale shark's gill (Fig. 1) is sufficient for a successful pattern recognition process [9].

In contrast to whales that are endothermic (warm blooded), sharks like other fishes are ectothermic (cold blooded) and needs to approach water surface to absorb energy and regulate their body temperature as shown by Thums et al. [10]. In fact, whales as breath-holding animals also go to the surface frequently, but basically for breathing. Whale sharks have a remarkable capability of thermoregulation [10]; in this regard, they come to the surface and swim to warm-up their body or dive into the depth to cool-down, i.e. energy dissipation. Meekan et al. reported that two whale sharks with a total length of 4 and 7 m in their study spent about 16-41% of their time within 5 m of the surface [11].

More recently Nakamura et al. studied body temperature stability of whale sharks. They showed that this gentle giant fish with a weight about 20 tons has a very small heat loss rate compared to other endothermic and ectothermic species [12,13]. This characteristic provides temperature stability for whale sharks during dives to cold depths sometimes exceeding 1000 meters without high metabolic cost [12].

On the other hand, eidonomic features existing on the external body surface of any marine creature considerably affect the way of its interaction with the aquatic environment, which in turn affect swimming behaviour and propulsion generation mechanism of the animal, like presence of tubercles having peaks and troughs with varying amplitude and wavelength on the leading edge of the humpback whale's flippers and flukes [14-17], presence of denticles on the shark skin [18], presence of longitudinal ridges on the carapace of leatherback turtles [19] and presence of ventral pleats on the belly of humpback whales [20], to name a few.

Formation of streamwise vortices is the key factor to understand underlying physics of the aforementioned problems. In these examples, streamwise vortices bring some extra momentum from relatively high-speed region outside of the boundary layer into the relatively low-speed zone via augmentation of fluid flow mixing and as a result supress/delay flow separations. For example, in the case of humpback whale's flippers, formation of two counter-rotating vortices around the trough of any protuberance at leading edge of the flipper leads to a softer post-stall behaviour [14-17]. As shown by Domel et al., denticles on the shark skin generate streamwise vortices that lead to a shorter reattached separation bubble, drag reduction over certain intervals of angle of attack (AoA hereafter) and maintaining higher hydrodynamic performance at high AoAs [18].

As clarified by Bang et al., streamwise vortices also play an important role in superior hydrodynamic performance of leatherback turtles in swimming [19]. In fact, five ridges over the animal's carapace generate streamwise vortices, which suppress separation bubble formation by locally favourable destabilization of flow field in the near-body zone. In the last case mentioned, ventral pleats on the belly of humpback whales result in the formation of low- speed strips with higher pressure on the bottom body surface of the animal, which generates lift and increases tendency of flow separation as shown by Taheri [20]; although in cavitating conditions, experienced by humpback whales in bubble net fishing circumstances, effect of ventral pleats is majorly suppressed [20].

In the present study as a branch of functional eidonomy research, it is shown that streamwise vortices are generated on the whale shark's ridges, which dominantly contributes to the flow physics. In this regard, unsteady flow over a scaled model of the whale shark body is numerically simulated at positive/negative AoAs and a prescribed sideslip angle. In the following, details are presented.

2. 'Whale Shark' Body Model

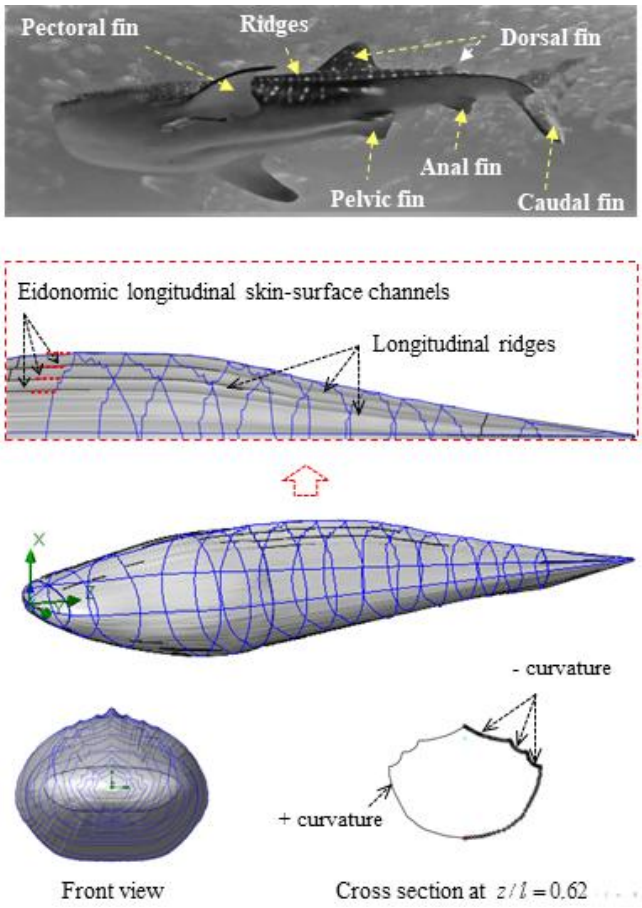

Figure 2. Whale shark's body morphology; Top: eidonomy (external morphology) details (modified from the base picture [22]), Middle-Bottom: a 3D biomimetic-scaled body model constructed in the present study, adopted for all upcoming CFD simulations

To construct a 3D body model of a whale shark (Fig. 2), cross-sections of a 1:40 scaled-down whale shark model are scanned and digitalized in selected planes perpendicular to the longitudinal (z) axis. Then, a total number of 16 cross-section curves and 4 guide curves forming the external shape of the whale shark body (in the mid-planes defined by

x=0 and y=0) are numerically generated by high resolution in MATLAB and imported to the SolidWorks CAD environment [23]. The final 3D numerical whale shark body model is majorly constructed by applying a lofting process, as shown in Fig. 2. The latter process is performed by stitching successive cross-section curves controlled by guide curves.

Whale shark normally has a total number of seven ridges on its sides which form six fluid flow channels over its body skin-surface. As shown in Fig. 2, external shape of any cross section of a whale shark body perpendicular to the longitudinal axis is convex with a positive Gaussian curvature; although the channels formed by two successive ridges represent local concave surfaces with negative Gaussian curvatures. As can be expected and is shown shortly, this interesting topology has direct fluid dynamical consequences in the locomotion of the animal in its aquatic habitat.

Geometrically, any channel formed by two successive neighbour ridges creates a diverging-converging flow passage with a varying angle and depth in the longitudinal direction starting approximately from the maximum height of the body extended to the caudal fin (Fig. 2). This special topology of channels is a bionic technique to generate streamwise vortices that can be observed with some variations in large-dominant scales over the whole body like ridges on whale shark's body (as shown in the present paper) and ridges on carapace of leatherback turtles [19] or in small-local scales like every single denticle on the shark's skin [18]. In fact, larger dominant streamwise vortices are generated in large-scale skin-surface channels, while in the case of shark's denticle, smaller local vortices are generated which effectively contributes to the drag reduction [18].

3. Numerical Methodology

To perform numerical flow simulations at a series of AoAs, α and sideslip angle ψ, the model is positioned at a fixed point in space and all above characterizing angles are implemented via freestream blowing angle with respect to the longitudinal z-axis (Fig. 3).

Inflow velocity is set based on a prescribed Reynolds number Re of the order of 10^7. In general, 'whale sharks' are among slow swimmers in oceans; as stated earlier these giants come to water surface for thermoregulation where a faster current exists about 2.5 m/s [24]. For instance, a 'whale shark' with a body length of 10 m that swims with a resultant speed of 5 km/h experiences fully turbulent flow over its body at $Re \approx 1.4\times10^7$. In this paper, all numerical simulations are performed at this Reynolds number. For simulations with imposing α, inflow velocity is applied as below:

$$\begin{aligned} u_x^{inflow} &= V_\infty.\sin(\alpha) \\ u_y^{inflow} &= 0 \\ u_z^{inflow} &= V_\infty.\cos(\alpha) \end{aligned} \quad (1)$$

while for numerical simulations with applying ψ, inflow is defined as below:

$$\begin{aligned} u_x^{inflow} &= 0 \\ u_y^{inflow} &= V_\infty.\sin(\psi) \\ u_z^{inflow} &= V_\infty.\cos(\psi) \end{aligned} \quad (2)$$

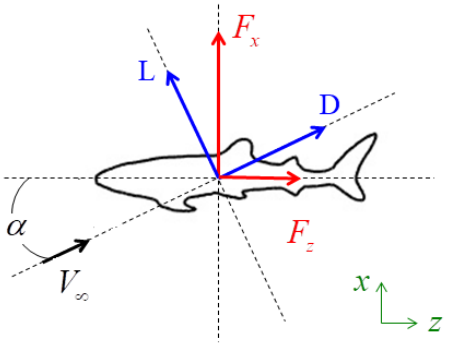

a) Angle of attack (AoA)

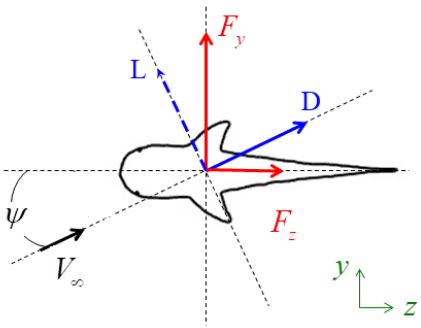

b) Sideslip angle

Figure 3. Coordinate system adopted for 'whale shark' flow simulations

3.1. Computational Domain and Grid Generation

Computational grids for numerical flow simulations are generated with the aid of SolidWorks meshing tools with capability of basic Cartesian mesh generation and applying an adaptive local grid filter to capture geometry of the ridges and boundary layers [25]. After performing grid convergence tests, a well-converged grid with 1.6 million elements is adopted here for all upcoming flow simulations. Fig. 4 and Fig. 5 show the computational mesh generated around the body model of a whale shark with ridges. It exhibits a well-resolved body-fitted mesh clustering to the wall to capture all details of the geometry. As shown at top of the figure, to minimize effects of the boundaries, the computational domain is extended about 3 and 4 times of the body length in x-y and z directions, respectively.

As one can see in Fig. 5, with three levels of clustering around the whale shark's body using adaptive meshing technique, a smooth transition between a relatively coarse mesh in the outer-flow region and the fine mesh in the near-body zone is obtained; which is desirable in terms of computational cost and accuracy.

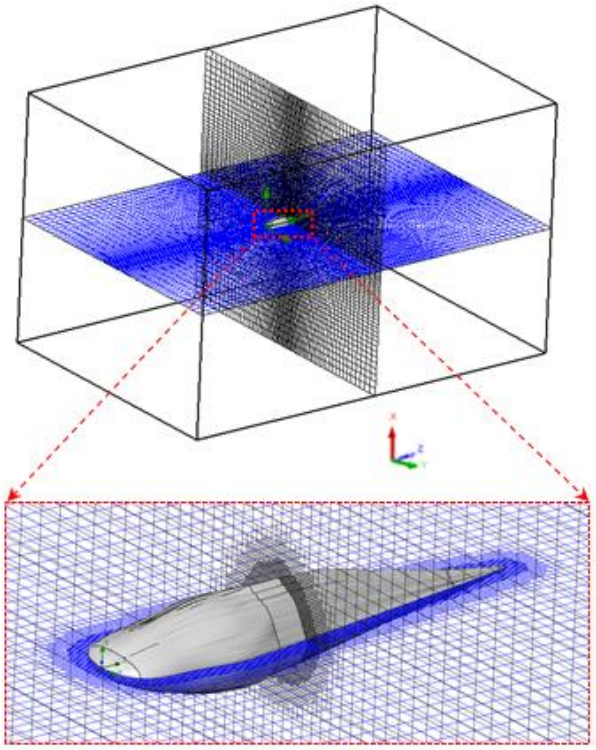

Figure 4. Computational domain with an adaptive grid generation around the 'whale shark's body model

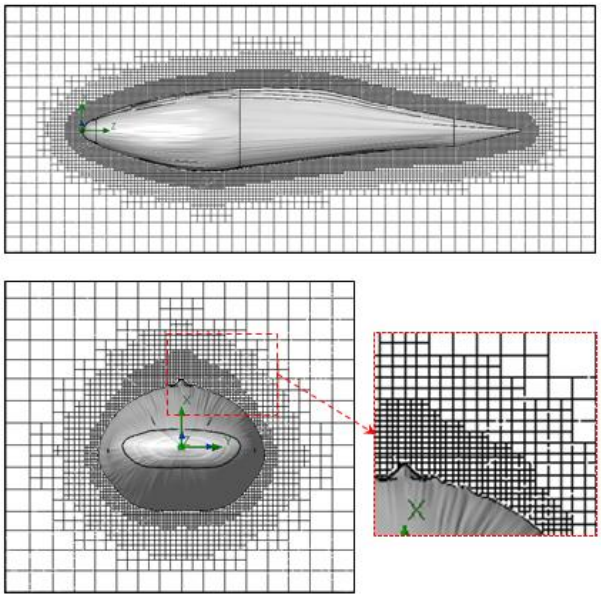

Figure 5. Computational grids at cross-sections in the middle planes: side view (top) and front view (bottom)

3.2. Turbulent Flow Treatment and Settings

Turbulent flow equations over the whale shark's body model are solved at $Re \approx 1.4\times10^7$ using unsteady Reynold averaged Navier-Stokes (URANS) technique [25]. In this regard, turbulence is treated with Lam- Bremhorst low-Reynolds number (LB LRN, hereafter) $k-\varepsilon$ model using SolidWorks Flow Simulation (SFS) solver [25,26]. The name of 'low-Reynolds number' here should not be confusing; in fact this refers to ability of the aforementioned model to treat low-speed boundary layers. This is achieved by taking into account wall-distances and using at least 10 computational nodes in the boundary layer [25]. In general, governing equations of the problem before applying Reynolds triple-decomposition can be expressed in Einstein tensor notation as below [25]:

$$\frac{\partial \rho}{\partial t}+\frac{\partial(\rho u_i)}{\partial x_i}=0 \tag{3}$$

$$\frac{\partial(\rho u_i)}{\partial t}+\frac{\partial(\rho u_i u_j)}{\partial x_j}=-\frac{\partial p}{\partial x_i}+\frac{\partial \tau_{ij}^*}{\partial x_j}+S^i \tag{4}$$

where S^i and τ^*, is defined as the following:

$$\tau_{ij}^*=2\left(\mu+\mu_t\right)S_{ij}-\frac{2}{3}\rho k\delta_{ij} \tag{5}$$

$$S_{ij}=\frac{1}{2}\left(\frac{\partial u_i}{\partial x_j}+\frac{\partial u_j}{\partial x_i}\right)-\frac{2}{3}\delta_{ij}\frac{\partial u_k}{\partial x_k} \tag{6}$$

μ_t and k is turbulent eddy viscosity and kinetic energy, respectively, while δ denotes the Kronecker delta. k and ε equations are coupled as follows [25,26]:

$$\begin{aligned}&\frac{\partial(\rho k)}{\partial t}+\frac{\partial(\rho u_i k)}{\partial x_i}=\frac{\partial}{\partial x_i}\left(\left(\mu+\frac{\mu_t}{\sigma_k}\right)\frac{\partial k}{\partial x_i}\right)\\&+\left(\tau_{ij}^*-2\mu S_{ij}\right)\frac{\partial u_i}{\partial x_j}-\rho\varepsilon\end{aligned} \tag{7}$$

$$\begin{aligned}&\frac{\partial(\rho\varepsilon)}{\partial t}+\frac{\partial(\rho u_i \varepsilon)}{\partial x_i}=\frac{\partial}{\partial x_i}\left(\left(\mu+\frac{\mu_t}{\sigma_\varepsilon}\right)\frac{\partial \varepsilon}{\partial x_i}\right)\\&+C_{\varepsilon1}f_1\left(\tau_{ij}^*-2\mu S_{ij}\right)\frac{\varepsilon}{k}\frac{\partial u_i}{\partial x_j}-C_{\varepsilon2}f_2\rho\frac{\varepsilon^2}{k}\end{aligned} \tag{8}$$

where parameters are adjusted, as below:

$$C_{\varepsilon1}=1.44,\ C_{\varepsilon2}=1.92,\ \sigma_k=1,\ \sigma_\varepsilon=1.3$$

To calculate μ_t, one can use the following formula:

$$\mu_t=f_\mu C_\mu \rho\frac{k^2}{\varepsilon} \tag{9}$$

In the above formula, $C_\mu \approx 0.09$ and f_μ, f_1 and f_2 are calculated as below:

$$\begin{aligned}&f_\mu=\left(1-e^{-0.0165R_y}\right)^2.\left(1+\frac{20.5}{R_t}\right)\\&f_1=1+\left(\frac{0.05}{f^\mu}\right)^3,\quad f_2=1-e^{R_t^2}\end{aligned} \tag{10}$$

where the parameters are defined as below:

$$R_y = \frac{\rho}{\mu} y\sqrt{k}, \quad R_t = \frac{\rho}{\mu}.\frac{k^2}{\varepsilon} \tag{11}$$

where y is the wall distance. Finally time and length scales are computed as below [27]:

$$L_t = \frac{k^{3/2}}{\varepsilon}, \quad T_t = \frac{k}{\varepsilon} \tag{12}$$

SFS solver uses finite-volume approach to solve fluid flow equations with the aid of computing methods like operator-splitting, conjugate gradient, multigrid and SIMPLE [23,25]. To solve water flows over the whale shark's body, inlet velocity is adjusted via equations (1) or (2); while other boundaries are set as 'outflows'. F_x, F_y and F_z forces acting on the whale shark's body by its interaction with the flow field are continuously monitored to ensure satisfaction of all convergence criteria. These measures are automatically applied by SFS solver based on dispersion of goal functions which leads to lowest residual errors [23].

4. Results and Discussion

In this section, results of numerical simulations of turbulent flows over the whale shark's body model are presented at $Re \approx 1.4\times10^7$. Validity of the numerical simulation strategy was confirmed in the previous study [20] by performing flow simulations over an ellipsoid at zero AoA and comparing drag coefficient with the experiment, $C_d \approx 0.06$. It was shown that applying an averaged roughness of 10 microns results in a good match to the experiment [20].

4.1. Effects of Ridges in Streamwise Swimming

In this subsection, streamwise swimming of the 'whale shark' at $\alpha = 0$ is considered. Fig. 6 shows convergence history of the vertical and axial forces. It is interesting to notice that presence of the prominent ridges on the whale shark's geometry and geometrical difference between top ($x > 0$) and bottom ($x < 0$) sections in the side-view profile of the animal (Fig. 7) breaks symmetry of the flow field. As one can see in Fig. 6, negative F_x is generated at $\alpha = 0$, which means whale shark's eidonomic shape generates a force opposite to the buoyancy or in the direction of the animal weight force. This feature also helps in what is so-called 'sinking feeling' of whale sharks, in accordance with experimental observations reported by Gleiss et al [28]. It is worth to mention that sharks do not have a 'swim bladder' like other fishes or Blubber fat layer under their skin like cetaceans or whales to facilitate their floating in water; instead their oily liver consists of oil/fats lighter than water that partially helps them to be afloat, but it is not enough and sharks have to swim continuously to avoid sinking. Gleiss et al. used a tagging technique to study movement strategies of whale sharks by recording some physical and environmental parameters. They observed that whale sharks take advantage of their negative buoyancy for gliding through descent movements from surface to the depths [28]. In another study, Gleiss et al. showed that negative buoyancy can be more efficient in the shark's accelerated movements [29].

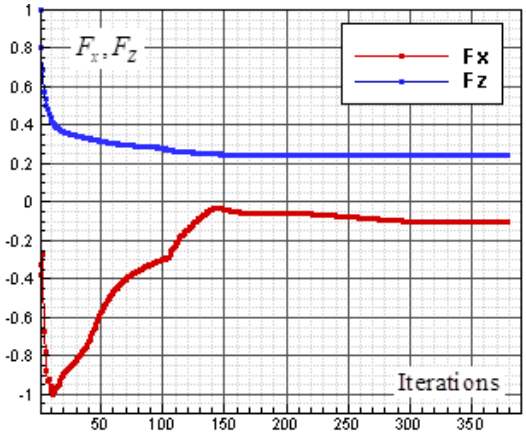

Figure 6. Convergence history of the normalized vertical and axial forces acting on the whale shark's body model at $\alpha = 0$

Fig. 7 depicts axial velocity field superimposed by pathlines in the middle section, defined as y=0. As one can see in the figure, flow accelerates in the first part of the whale shark's body profile from its nose to the maximum height (thickness) of the body. In the aft section of the body, a wake region forms with relatively low-speed compared to the outer flow region. Although no separation zone with $u_z < 0$ is generated, thanks to the streamlined profile of the body and presence of the prominent ridges.

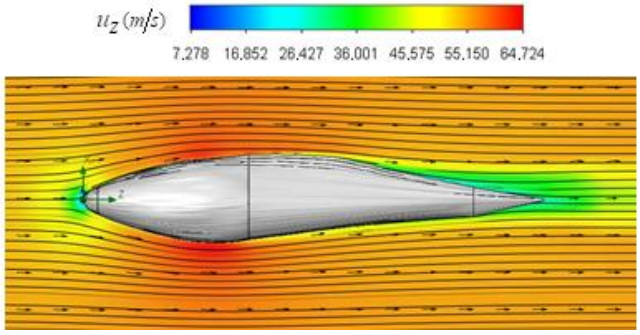

Figure 7. Axial velocity field around the whale shark's body at $\alpha = 0$ in the middle plane defined as y=0

In general, to identify vortex cores with/without shear contamination in flow fields, λ_2-criterion with a threshold defined as $\lambda_2 < 0$ can be utilized [30]. Practically, an appropriate value of the threshold level is case-dependent. Fig. 8 represents hidden structures generated on the whale shark's body model extracted by $\lambda_2 = -10^5$. As one can see in the figure, streamwise vortices are generated by special topology of the prominent ridges on the whale shark's body. It can be postulated that presence of these streamwise vortices injects some extra momentum from higher velocity region into the near-body zone with lower velocity and suppresses or delays separation.

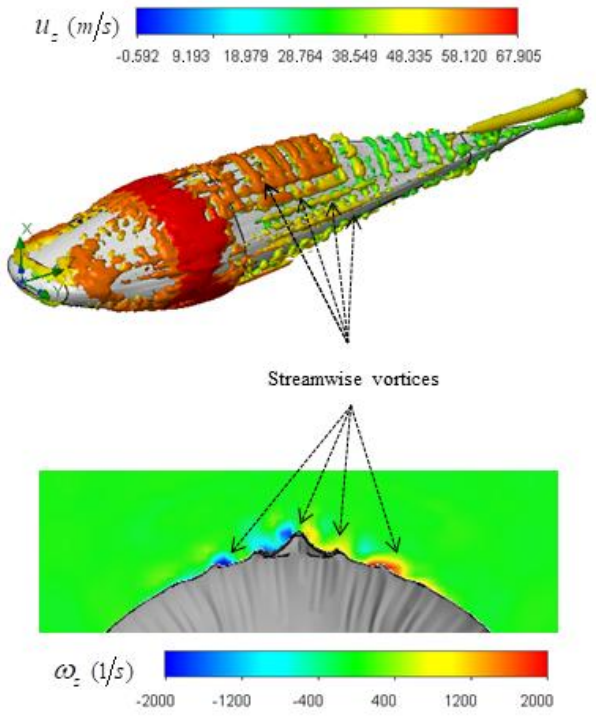

Figure 8. Vortical structures/shear layers developed on the whale shark's body model captured by λ_2 -criterion at $\alpha = 0$, isometric view (top); streamwise vorticity generated by the prominent ridges on the whale shark's body model (bottom)

4.2. Effects of Ridges in AoA

As mentioned before, whale sharks are gentle swimmers with not relatively high physical activities in oceans and their swimming speed can be considered $5\,km/h$ in average and can ultimately reaches to $13\,km/h$ over a short period of time as reported by Hsu et al. [4]. This range of speeds in combination with ocean current speeds having maximum value of $2.5\,m/s$ near the surface creates a broad range of AoAs and sideslip angles. This is important to be considered because whale sharks spend a relatively large period of time near the ocean surface for thermoregulation. In this subsection, turbulent flows over the whale shark's body are simulated at $\alpha = 0, \pm 30^\circ, \pm 60^\circ$ and $\psi = -45^\circ$.

Fig. 9 shows variation of lift and drag coefficients of the whale shark's body versus AoA for all performed numerical simulations in this subsection. As one can see in the figure, symmetry breaks for positive and negative AoA counterparts; although similarity exists between two cases. It is worth to mention that drag and lift coefficients are calculated here based on the body's planform area. In the literature, experimental drag coefficient data for a 3D streamlined body is equal to 0.04 based on frontal area for $Re > 10^5$ at $\alpha = 0$ [31]; considering geometry of whale shark's body and using planform area, instead of frontal area, drag coefficient is calculated as 0.014. Simulation results show that drag coefficient is augmented to 0.015 calculated based on the planform area at $\alpha = 0$, due to an increase in the wetted area.

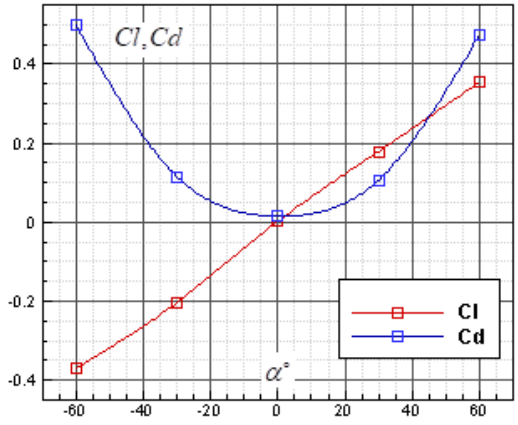

Figure 9. Life and drag coefficients based on planform area generated by the whale shark's body model at different AoAs at $Re = 1.4 \times 10^7$

Fig. 10 and Fig. 11 depict convergence history of the normalized vertical and axial forces at $\alpha = \pm 30^\circ$ and $\alpha = \pm 60^\circ$, respectively. By comparing of these figures, it is clear that absolute values of the converged values of vertical and axial forces increase by increasing AoA.

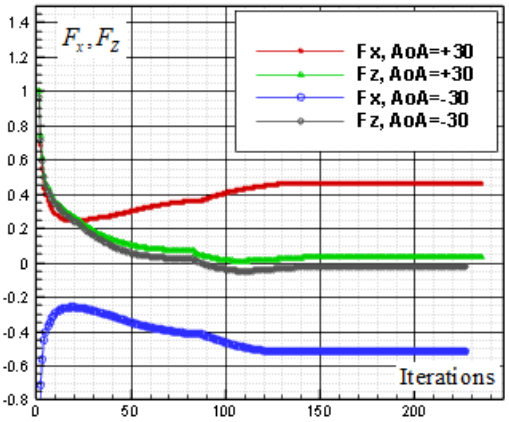

Figure 10. Convergence history of the normalized vertical and axial forces acting on the whale shark's body model at $\alpha = \pm 30^\circ$

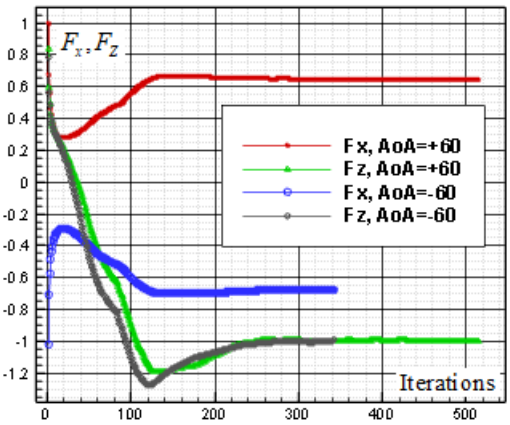

Figure 11. Convergence history of the normalized vertical and axial forces acting on the whale shark's body model at $\alpha = \pm 60^\circ$

Fig. 12 shows topology of the flow fields at different AoAs. Basically more complex pattern is generated due to bundling of flow pathlines over the whale shark's body at higher AoA. This originates from existing vortical structures in the animal's wake (Fig. 14). As shown in Fig. 12, symmetry between $\alpha = \pm 60^{\circ}$ cases no longer exist; in $\alpha = -60^{\circ}$, there exists a heavier wake and a wider bundled pathlines compared to $\alpha = +60^{\circ}$. Presence of ridges on the dorsal and lateral sides of the animal majorly modifies topology of the flow fields. For $\alpha = \pm 30^{\circ}$ cases, the abovementioned effect is present but less pronounced.

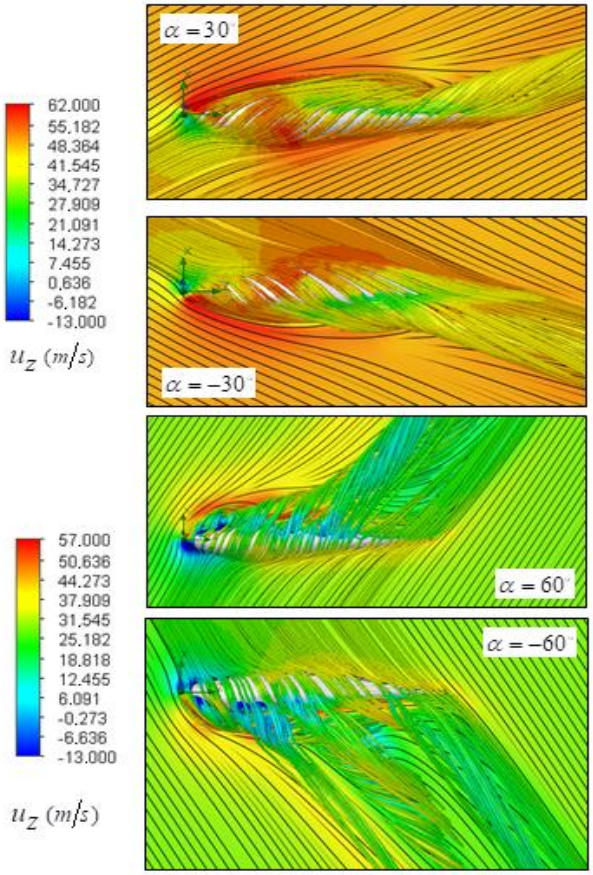

Figure 12. 3D pathlines over the whale shark's body model along with axial velocity fields at different AoAs in the middle plane defined as y=0

Fig. 13 shows the average axial velocity field around body of the whale shark model at $\alpha = +60^{\circ}$. As one can see in the figure, two dominant counter-rotating vortices are generated on top of the whale shark's body. These vortical structures lead to formation of regions with high and low axial velocities close together on top of the body, as shown in the figure. It is interesting that these rotating regions are detached from the whale shark's body in a way that two saddle-points are clearly formed in the pathlines map.

To further investigate underlying physics of the problem, vortical structures developed on the whale shark's body model are extracted using λ_2 -criterion. Fig. 14 depicts vortical structures developed on the whole body of the whale shark. As can be expected and shown in the figure, different 3D patterns of vortical structure developments exist at different AoAs. As depicted in the figure, structures start to be shaped from the animal's nose at all AoAs. For positive angles, structures are more pronounced on the top of the whale shark's body, while for the negative angles, structures are more dominant on the bottom part of the body.

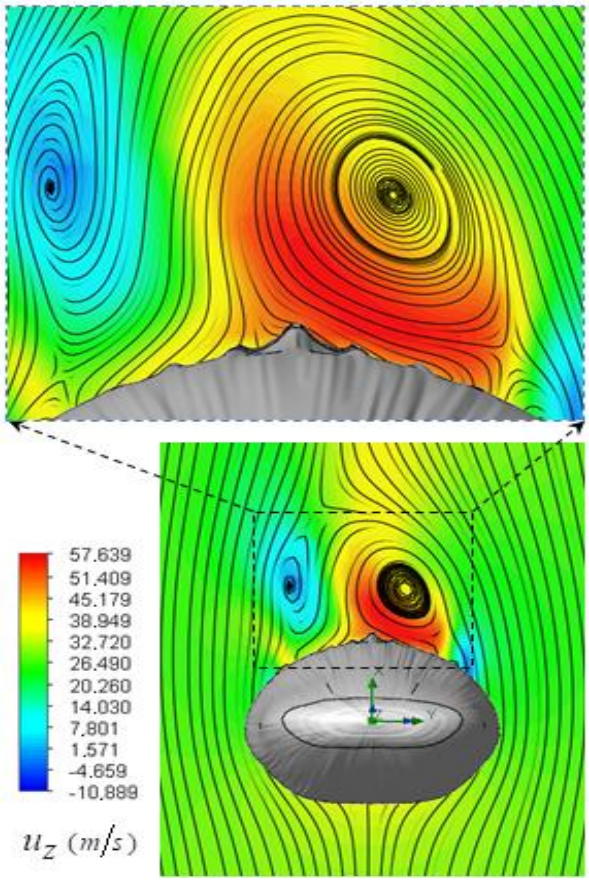

Figure 13. Mean axial velocity field around the whale shark's body at $\alpha = +60^{\circ}$ in the middle plane at z/L=0.5, where (L) denotes the body length; pathlines close to the body (top), front view field (bottom)

At $\alpha = \pm 30^{\circ}$, two distinct tail-like vortical structures attached to the whale shark's body corresponding to vortex cores with minimum pressure are generated extending downstream with a slope angle equals to the imposed AoA. By increasing of AoA to $\alpha = 60^{\circ}$, more vortical/ shear layer structures are generated on the body as expected apriori. As it is visible in the figure, at $\alpha = \pm 60^{\circ}$ detached coherent structures are also captured by λ_2-criterion which can be linked with strength of the aforementioned structures and the threshold values; in general by increasing absolute value of λ_2, fewer structures with higher strength are captured. By comparing $\alpha = \pm 60^{\circ}$ cases, it is observed that at negative AoA concentration of the flow structures with strong rotation centers decreases compared to the positive AoA, this fact is also visible in the 3D pathlines embracing the body illustrated in Fig. 14. As one can also conclude, due to presence of the prominent longitudinal ridges and dissymmetry which basically exists between the top and

bottom of the whale shark's body profile, vortical structures generated on the body should be different, although similar.

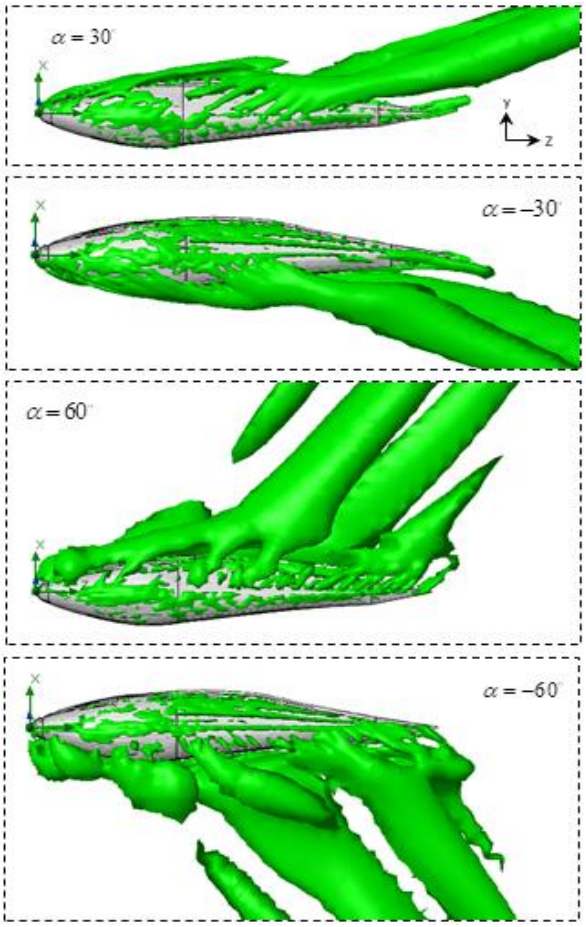

Figure 14. Vortical/shear layer structures developed on the whale shark's body model at different AoA, extracted with $\lambda_2 = -10^5$

4.3. Effects of Ridges in Sideslip Angles

As mentioned before, whale sharks experience sideslip angles while swimming, majorly induced by surface currents and whale shark's gentle activities. In this subsection, at a relatively high sideslip angle, $\psi = -45^\circ$, turbulent flow over the whale shark's body model is numerically simulated at $Re \approx 1.4\times10^7$. Fig. 15 shows convergence history of the normalized forces acting on the whale shark's body by passing turbulent flow at the sideslip angle. As one can see in the figure, due to presence of ridges on the dorsal-lateral parts of the body and geometrical dissymmetry of the eidonomic shape of whale sharks in the vertical direction (x-axis), negative F_x is majorly generated (opposite to buoyancy force), which profoundly contributes to the 'sinking feeling'.

Fig. 16 depicts that vortical structures are deflected due to applying a -45° sideslip angle. As shown in the figure, a dominant vortical structure corresponding to a strong vortex core is majorly generated on the left-side of the body (i.e., downstream) originating from the body mid-section. Although, a smaller vortical structure is also present at the aft zone of the whale shark's body at this sideslip angle. Some non-coherent vortical structures with sparse distribution are captured on the right-side of the body.

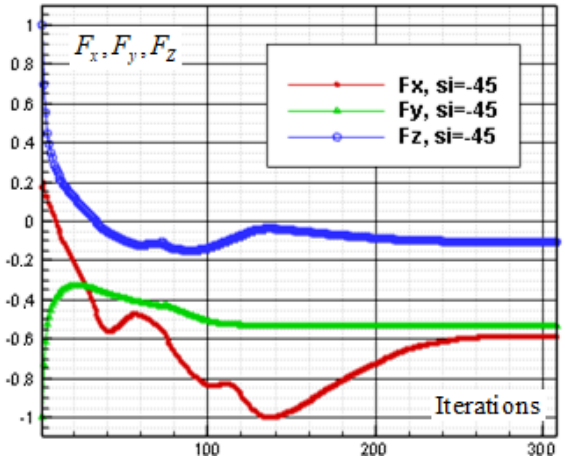

Figure 15. Convergence history of the normalized vertical, lateral and axial forces acting on the whale shark's body model at $\psi = -45^\circ$

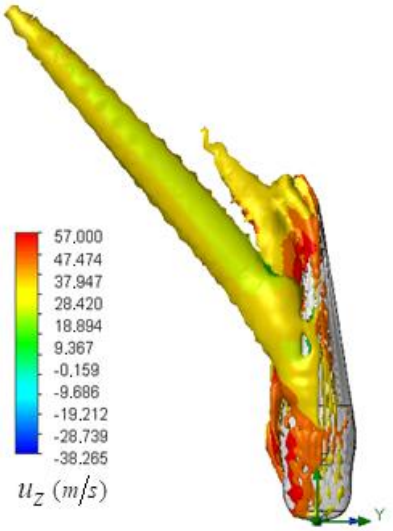

Figure 16. Vortical/shear layer structures developed on the whale shark's body model at sideslip angle $\psi = -45^\circ$ captured by $\lambda_2 = -10^5$

Fig. 17 shows pathlines over the whale shark's body model at different cross-sections perpendicular to the axial (z) axis obtained from mean axial velocity fields at the sideslip angle. As one can see in the figure, there exists a remarkable change in the eidonomic shapes of the whale shark's cross-sections in the longitudinal direction. Obviously, this has serious fluid dynamical consequences, which can be seen in the flow filed topologies (Fig. 17). As shown in the figure, by increasing z/L, irregularity of the cross-section increases in a way to get farther away from the circular shape and sharp corners are formed; furthermore presence of these ridges makes it more complicated in a sense. At z/L=0.5 and 0.8, a dominant vortex is generated which is at the top of the body covering a low-speed region and close to the bottom of the body with high-speed, respectively. These average pictures

show formation of the saddle points in the pathlines pattern at these two sections. At z/L=0.3, no dominant vortex and also no separation zone is produced in the flow field. These averaged fields also suggest that presence of the prominent ridges can modify formation of reverse von Kármán vortex street and vortex shedding characteristics of the whale shark's tail. More details are presented in subsection (4.5).

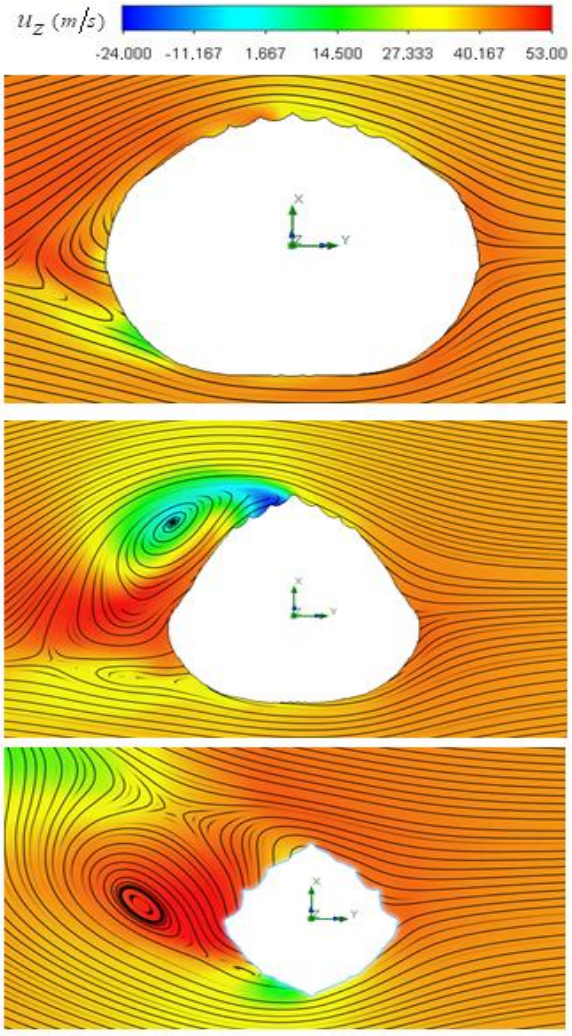

Figure 17. Mean axial velocity field around the whale shark superimposed with flow pathlines at $\psi = -45^{\circ}$ in the vertical planes defined from top to bottom as z/L= 0.3, 0.5 and 0.8; where (L) denotes the body length

4.4. Predicted Separation Zones

Fig. 18 illustrates the mean flow separartion zones defined as iso-surfaces of reverse flows obtained from turbulent flow simulations over the whale shark's body.

As one can see in the above figure, separation zones on the whale shark's body are getting larger by increasing AoA. At $\alpha = \pm 30^{\circ}$, separation zones are only limited to the nose of the marine animal. By increasing AoA to $\alpha = \pm 60^{\circ}$, separation zones are visible at whale shark's nose for both angles; non-coherent sparse separation zones are majorly generated on top and bottom of the body at positive and negative AoA, respectively. At the sideslip angle, relatively small separation zone forms on the left side of the whale shark's body.

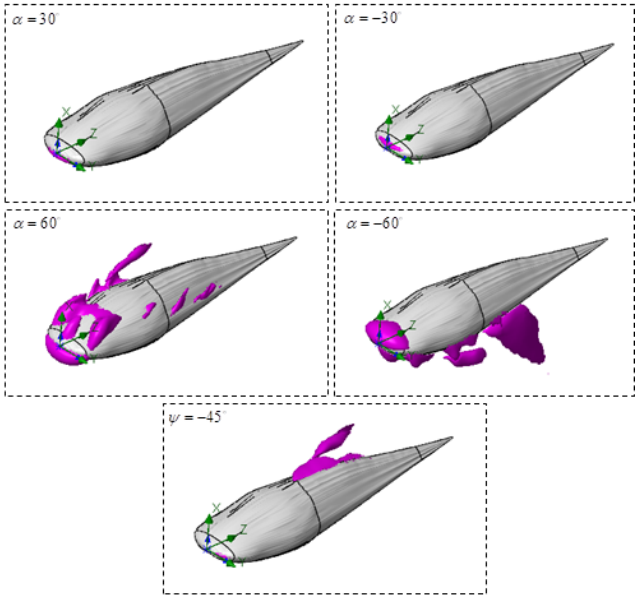

Figure 18. Separation zones formed on the whale shark's body model at different AoA and sideslip

4.5. Effects of Ridges on Tail Beating Hydrodynamics

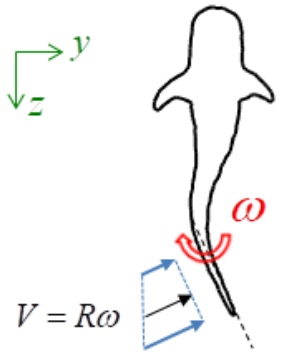

Figure 19. A simplified model for start-up tail beating of a 'whale shark' in a quiescent flow environment

Whale sharks use undulatory/oscillatory movements of their aft-body/ tail (typically exceeding caudal peduncle zone) and large vertical caudal fin from side to side for propulsion generation. Their caudal fin size from its top-tip to the bottom-tip is about 1/3 of their total body length. To have an idea how presence of the prominent ridges modifies hydrodynamics of the tail-beating, here an unsteady simulation of start-up phase of the whale shark's tail beating in a quiescent flow environment is considered. Fig. 19 illustrates a simplified model of the problem. It is assumed in the model: by tail beating, whale sharks move aft-part of the body/tail and caudal fin in a rotation with a constant frequency about a pivot point forming an arm with a length equals to a given percentage of the body length. In the model, by tail beating a linear velocity distribution is generated as $V = R\omega$; where R is length of the arm and ω is the angular

velocity of the tail beating. One can rewrite the above equation as $V = \omega(r - r^{\dagger})$; where r is a local arm length variable defined at any point on the tail and $r^{\dagger}$ is the position of the assumed pivot point on the body.

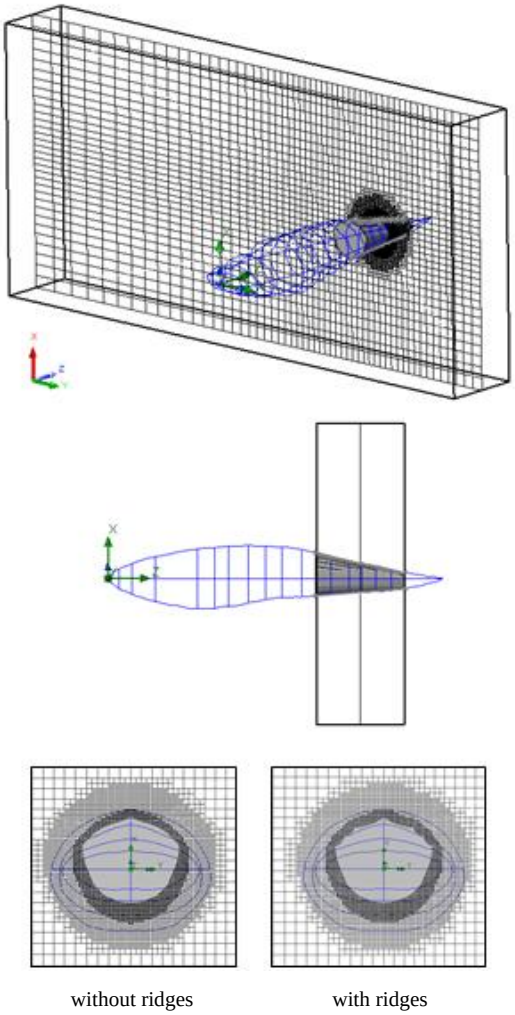

Figure 20. Computational domain and grid generation around the whale shark's tail with/without ridges

To investigate effects of the ridges on the tail beating of a whale shark using the aforementioned model, tail-only flow simulations are performed with variable inlet boundary condition. In this regard, two models of the tail with/without ridges are constructed. Fig. 20 shows the computational domain and grid generated around the two geometries. To minimize effects of the boundaries, computational domain is symmetrically extended 1.7 times of the tail length in x-direction and unsymmetrically in y direction, i.e. 1.5 times in the upstream direction and 5.5 times in the downstream direction to capture wake of the tail properly (Fig. 20). After performing grid convergence tests, a well-converged grid with 0.8 million elements is adopted for unsteady simulations in this subsection. As one can see in the figure, like before three levels of refinements could result in a smooth transition between the outer coarse mesh to the near-body fine mesh. The prominent ridges are also captured properly by the generated grid. To perform unsteady simulations here, linear inlet boundary condition is imposed at the upstream inlet section as explained earlier; all other boundaries are set as 'outflows' as the previous simulations. Both simulations are initiated from the same initial conditions with $\Delta t = 10^{-3} s$.

As stated before, numerical simulation here is limited to the undulatory part of the body/tail, thus the computational domain in the model is extended from the pivot point assumed here at $r^{\dagger} / L = 0.7$. Meekan et al. reported frequency and amplitude of the tail beating of two 4 and 7 meter whale sharks, which represents a linear variation between modal frequency and amplitude of the whale shark tail beating for propulsive strokes [11]. For unsteady simulations in this subsection, $\omega \approx 0.2\ Hz$ is applied.

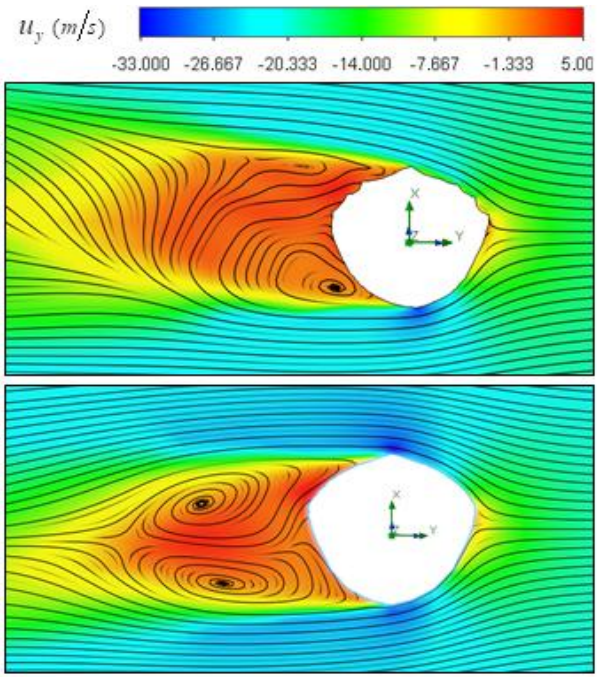

Figure 21. Mean lateral velocity field and pathlines over the whale shark's tail at z/L= 0.75; where (L) denotes the body length; with ridges (top), without ridges (bottom)

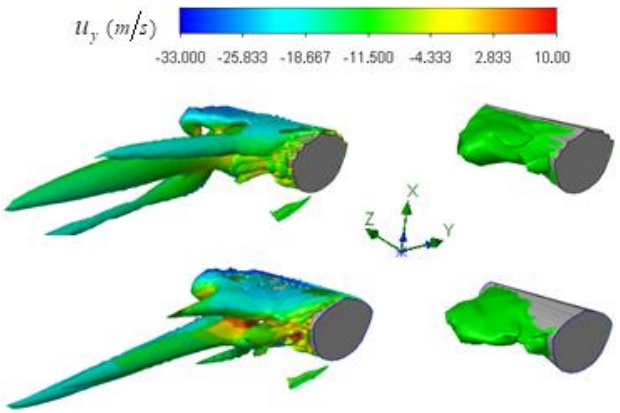

Figure 22. Mean vortical structures developed on the whale shark's tail (left); separation zones (right): with (top) /without (bottom) ridges

Fig. 21 shows mean lateral velocity fields and pathlines over the whale shark's tail with/without ridges at z/L= 0.75 obtained from the time-dependent simulations. As one can see in the average field, presence of the ridges profoundly modifies topology of the flow field and formation of vortical structures around the tail. Thus the generated von Kármán vortex street are majorly modified by these ridges.

In the case of the whale shark's tail without ridges, two counter-rotating vortices are generated in the wake/ separation zone of the tail in the average flow as shown in Fig. 21. This classical picture is modified due to presence of the prominent ridges in whale sharks; as one can see in the figure only one large vortex is present in the wake with a vortex core close the tail bottom far from the ridges. Fig. 22 also depicts separation zones (Iso-surfaces of $u_y > 0$) and vortical structures formed in the tail beating. As shown in the figure, some strong vortex cores are captured by $\lambda_2 = -10^5$ in a reference frame positioned on the whale shark's tail. The figure shows that presence of the ridges modifies details and global features of the flow fields.

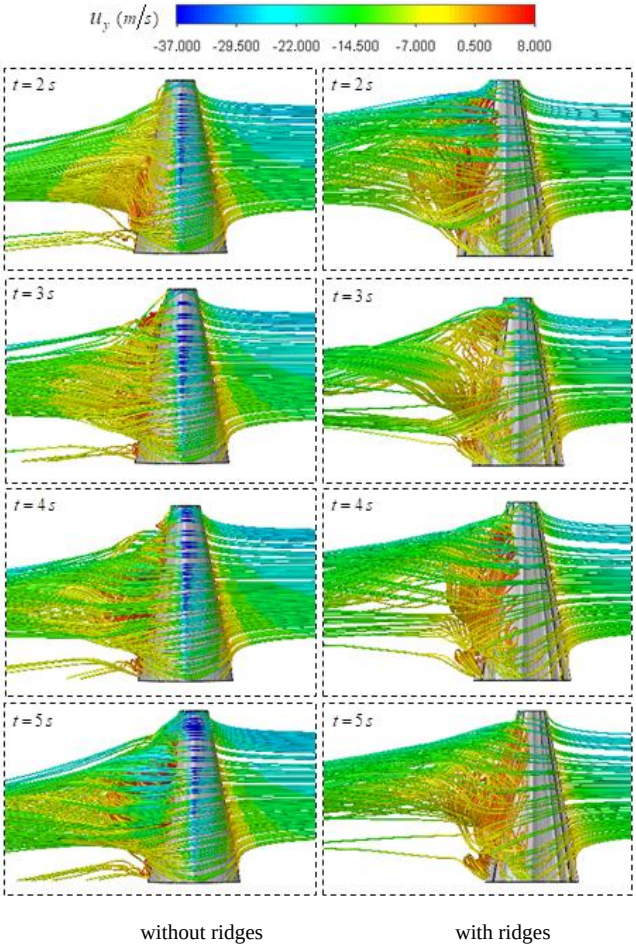

Figure 23. Unsteady 3D pathlines in the start-up phase of a whale shark's tail beating in a quiescent flow with ridges (right) and without ridges (left)

To grasp a better insight about time-dependent effects of the ridges in tail beatings of a whale shark, Fig. 23 shows temporal variation of 3D pathlines over the tail. As one can see in the figure, temporal dynamics of the vortical structures in the separation zones and wakes of the caudal peduncle are remarkably modified by presence of the prominent longitudinal ridges.

To further investigate the problem, energy content of the lateral velocity signals for the cases with/without ridges are also considered. Fig. 24 illustrates the physical positions of the probe points utilized in this study for velocity signal monitoring in respect to the body profile location.

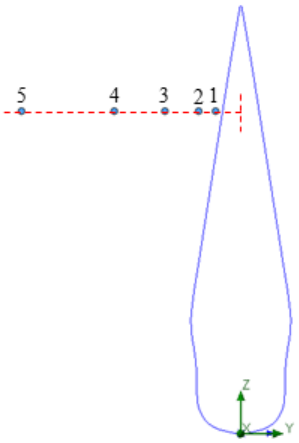

Figure 24. Probe points adopted for lateral velocity signal sampling

Table 1 also presents coordinates of the hired probe points all located in the computational domain generated around the whale shark's tail (Fig. 20) on a lateral line perpendicular to the axial body axis of the whale shark (Fig. 24).

Table 1. Normalized probe positions in the lateral direction (Figure 24)

Probe No.	x/L	y/L	z/L
1	0.013	-0.06	0.75
2	0.013	-0.10	0.75
3	0.013	-0.18	0.75
4	0.013	-0.30	0.75
5	0.013	-0.52	0.75

Fig. 25 shows power spectral density (PSD) of the lateral velocity signals sampled at 5 probe points introduced in Table 1. Sampling was performed at every time step ($\Delta t = 10^{-3} s$) for a total physical-time duration of $3s$. In this regard, sampling process was started after passage of $2s$ start-up phase spent to achieve a statistical convergence state. As one can see in the figure, for all probe points presence of the ridges makes the energy curves more uniform via suppressing of the positive/negative peaks of the curves; in this way ridges behave as an efficient energy damper for vortical structures originating from caudal peduncle zone. In this way, large vortical structures with maximum energy (marked by dashed-circles in Fig. 25) are effectively removed by the ridges. As one can also see in the figure, only dominant unsteadiness in the flow field can ultimately be seen in URANS technique as adopted in this

paper. To further investigate effects of the ridges on turbulent eddies and reproduce turbulence spectrum in full with -5/3 decay in the inertial subrange, full/semi- resolving techniques like DNS, LES or DDES should be utilized in future to resolve eddies, although by spending more computational costs.

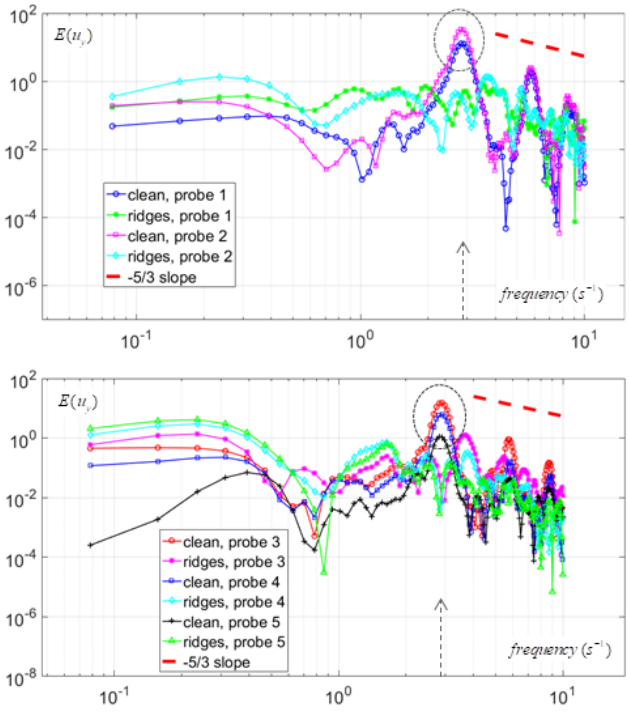

Figure 25. PSD of the lateral velocity signals captured by probes (Table 1) in the tail/caudal peduncle region of a whale shark

5. Conclusions

This paper shed some light on the hydrodynamic effects of the prominent ridges as an eidonomic feature on locomotion of the largest known fish on the planet. It was discussed that each two successive neighbour ridges with its special geometry create a so-called 'fluid flow channel' on the whale shark's skin; these 6 diverging-converging channels with variable depths in the longitudinal direction act as a bionic structure for generation of streamwise vortices. These vortices in turn minimize formation of the separation zones.

Numerical simulations in the streamwise swimming also showed that, a downward force (opposite to the buoyancy) is generated although small, by the external shape of the whale shark which contributes to the so-called 'sinking feeling'. Especially at swimming with sideslip angle, a noticeable amount of force acting on the whale shark body is generated by the ridges in the direction opposite to the buoyancy, which clearly contributes to the 'sinking feeling'. This geometry-induced negative-buoyancy feature along with the default negative-buoyancy of sharks can be potentially used by whale sharks for very fast diving to the depths. As simulations show, this can be simply performed by adjustment of the whale shark's heading with a sideslip angle while swimming. Numerical simulations at different AoA and sideslip showed that presence of ridges considerably modifies flow structures formed in the flow field. Thanks to streamlined body shape of the whale sharks and presence of the prominent ridges on their body, flow separations are limited to small zones on the body.

Unsteady simulations of whale shark's tail beating model showed that presence of ridges radically modifies characteristics of vortical structures originating from the caudal peduncle zone. PSD analysis showed that energy content of the dominant vortical structures is noticeably modified by the ridges and peaks of the energy curves are suppressed. In this view, the ridges act as bionic energy dampers for vortical structures originating from the caudal peduncle zone.

ACKNOWLEDGEMENTS

The author would like to sincerely acknowledge every single effort done by institutes, organizations and individuals to protect 'whale sharks' worldwide.

REFERENCES

[1] J. A. McKinney, E. R. Hoffmayer, J. Holmberg, R. T. Graham, W. B. Driggers, R. de la Parra-Venegas, B. E. Galvan-Pastoriza, S. Fox, S. J. Pierce and A. D. M. Dove, "Long-term assessment of whale shark population demography and connectivity using photo-identification in the Western Atlantic Ocean", PLoS ONE, vol.12, no.8, e0180495, 2017.

[2] M. G. Meekan, C. J. A. Bradshaw, M. Press, C. McLean, A. Richards, S. Quasnichka and J. G. Taylor, "Population size and structure of whale sharks Rhincodon typus at Ningaloo Reef, Western Australia", Marine Ecology Progress Series, vol.319, pp.275–285, 2006.

[3] G. Araujo, A. Agustines, B. Tracey, S. Snow, J. Labaja and A. Ponzo, "Photo-ID and telemetry highlight a global whale shark hotspot in Palawan, Philippines", Scientific Reports, Nature Journal, vol.9, no.17209, doi: 10.1038/ s41598- 019-53718-w, 2019.

[4] H. H. Hsu, S. J. Joung, Y. Y. Liao, K. M. Liu, "Satellite tracking of juvenile whale sharks, Rhincodon typus, in the Northwestern Pacific", Journal of Fisheries Research, vol.84, no.1, pp.25-31, 2007.

[5] A. Djunaidi, J. Jompa, Nadiarti, A. Bahar, A. Sianipar, A. W. Hasan, I. S. Alaydrus and M. Erdmann, "Potential tourism development for whale shark (Rhincodon typus) watching in eastern Indonesia", IOP Conf. Series: Earth and Environmental Science, vol. 253, 2019.

[6] D. P. Robinson ,M.Y. Jaidah, S. S. Bach, C.A. Rohner, R.W. Jabado, R. Ormond and S. J. Pierce, "Some like it hot: Repeat migration and residency of whale sharks within an extreme natural environment", PLoS ONE, vol.12, No.9, e0185360, 2017.

[7] L. Copmpagno, M. Dando and S. Fowler, "Sharks of the world", Princeton University Press, New Jersey, 2005.

[8] C. R. McClain, M. A. Balk, M. C. Benfield, T. A. Branch and C. Chen, "Sizing ocean giants: patterns of intraspecific size variation in marine megafauna", PeerJ Journal, doi: 10.7717/peerj.715, 2015.

[9] Wildbook for whale sharks photo-identification library, Wild Me Project, http://whaleshark.org, 2020.

[10] M. Thums, M. Meekan, J. Stevens, S. Wilson, and J. Polovina, "Evidence for behavioural thermoregulation by the world's largest fish", Journal of Royal Society Interface, vol. 10, no.20120477, 2014.

[11] M. G. Meekan, L. A. Fuiman, R. Davis, Y. Berger and M. Thums, "Swimming strategy and body plan of the world's largest fish: implications for foraging efficiency and thermoregulation", Frontiers in Marine Science, vol.2, no.64, doi: 10.3389/fmars.2015.00064, 2015.

[12] I. Nakamura, R. Matsumoto and K. Sato, "Body temperature stability in the whale shark, the world's largest fish", Journal of Experimental Biology, vol.223, jeb210286, doi: 10.1242/ jeb.210286, 2020.

[13] K. Knight, "It's cold out, but whale sharks stay warm within", Inside JEB- Journal of Experimental Biology, vol.223, doi:10.1242/jeb.227900, 2020.

[14] D. S. Miklosovic, M. M. Murray, L. E. Howle and F.E. Fish, "Leading-edge tubercles delay stall on humpback whale (Megaptera novaeangliae) flippers", Physics of Fluids, vol. 16, pp.39 – 42, 2004.

[15] A. Taheri, "A meta-model for tubercle design of wing planforms inspired by humpback whale flippers", International Journal of Aerospace and Mechanical Engineering, vol.12, no.3, pp.315-328, 2018.

[16] N. Rostamzadeh, K. L. Hansen, R. M. Kelso and B. B. Dally , "The formation mechanism and impact of streamwise vortices on NACA 0021 airfoils performance with undulating leading edge modification", Journal of Physics of Fluids, v.26, n.107101, 2014.

[17] K. L. Hansen, R. M. Kelso, B. B. Dally and E. R. Hassan, "Analysis of the streamwise vortices generated between leading edge tubercles", 6th Australian Conference on Laser Diagnostics in Fluid Mechanics and Combustion, Canberra, Australia, 5–7 December, 2011.

[18] A. G. Domel, M. Saadat, J. C. Weaver, H. Haj-Hariri, K. Bertoldi and G.V. Lauder, "Shark skin-inspired designs that improve aerodynamic performance", Journal of Royal Society Interface, vol.15, no.20170828, 2018.

[19] K. Bang, J. Kim, S. I. Lee and H. Choi, "Hydrodynamic role of longitudinal dorsal ridges in a leatherback turtle swimming", Scientific Reports, Nature Journal, vol.6, no. 34283, doi:10.1038/srep34283, 2016.

[20] A. Taheri, "On the hydrodynamic effects of humpback whale's ventral pleats", American Journal of Fluid Dynamics, vol.8, no.2, pp.47-62, 2018.

[21] S. P. Lambarri, Whale shark swimming - Maldives, https:// unsplash.com/.

[22] S. Hao, Whale shark swimming in an aquarium, https:// unsplash.com/.

[23] SolidWorks, Software Package, Dassault Systemes, SolidWorks Corp., Concord, MA, 2016.

[24] National Science Service Data, National Oceanic and Atmospheric Administration, U.S. Department of Commerce.

[25] A. Sobachkin and G. Dumnov, "Numerical basis of CAD-Embedded CFD", NAFEMS World Congress, Dassult Systems Inc., 2013.

[26] C. K. G. Lam and K. A. Bremhorst, "A modified form of the k-e model for predicting wall turbulence", Journal of Fluid Engineering, vol.103, pp. 456–460, 1981.

[27] S. Pope, "Turbulent flows", Cambridge University Press, 2004.

[28] A. C. Gleiss, B. Norman and R. P. Wilson, "Moved by that sinking feeling: variable diving geometry underlies movement strategies in whale sharks", Journal of Functional Ecology, vol.25, pp.595–607, 2011.

[29] A. C. Gleiss, J. Potvin and J. A. Goldbogen, "Physical trade-offs shape the evolution of buoyancy control in sharks", Journal of Royal Society B., vol.284, no. 20171345, 2017.

[30] J. Jeong and F. Hussain, "On the identification of a vortex", Journal of Fluid Mechanics, vol.285, pp.69-94, 1995.

[31] B. R. Munson, D. F. Young, T. T. Hisao Okiishi, "Fundamentals of fluid mechanics", John Wiley & Sons Australia Limited Publication, 2002.